CMS Physics Analysis Summary

Contact: cms-pag-conveners-smp@cern.ch 2013/04/23

Measurement of the differential and double-differential Drell-Yan cross sections in proton-proton collisions at $\sqrt{s} = 7$ TeV

The CMS Collaboration

Abstract

Measurements are presented for the measurements of the differential and double differential Drell-Yan cross section using an integrated luminosity of 4.5 fb^{-1} (dimuon) and 4.8 fb^{-1} (dielectron) of proton-proton collision data recorded with the CMS detector at the LHC at $\sqrt{s} = 7$ TeV. The cross sections $d\sigma/dM$ are measured in the mass range 15 GeV to 1500 GeV for the dimuon, dielectron, and combined channels. Results are also presented on the measurement of the double-differential cross section $d^2\sigma/dMdY$ in the dimuon channel. The double-differential cross section measurement is performed over the mass range 20 GeV to 1500 GeV and absolute dimuon rapidity from 0 to 2.4. The differential cross section measurements are normalized to the Z-peak region ($60 - 120$ GeV) to achieve better accuracy. The measurements are compared to the predictions of perturbative QCD calculations at next-to-leading and next-to-next-to-leading order using various sets of parton distribution functions.

Contents

1 Introduction

Drell-Yan lepton-pair production in hadron-hadron collisions is described in the standard model by s-channel γ^*/Z exchange. Theoretical calculations of the differential cross section $d\sigma/dM$ and the double-differential cross section $d^2\sigma/dMdY$, where M is the dilepton invariant mass and Y is the absolute value of the dilepton rapidity, are well established up to the next-to-next-to-leading order (NNLO) in quantum chromodynamics (QCD) [1–3]. The rapidity distributions of the gauge bosons are sensitive to the partonic content of the proton, and the very high energy of the Large Hadron Collider (LHC) allows the parton distribution functions (PDFs) to be probed in regions of Bjorken x scaling variable and rapidity Y not previously accessible in hadron colliders. The rapidity Y of the dilepton produced in proton-proton collisions is related to the momentum fraction x_+ (x_-) carried by the parton in the forward-going (backward-going) proton as described by the leading-order formula $x_\pm = \frac{M}{\sqrt{s}}e^{\pm Y}$. Therefore, the rapidity distribution directly reflects the PDFs of the interacting partons. The measurements of the double-differential cross section $d^2\sigma/dMdY$ in Drell-Yan and W production are particularly important since they provide tests of perturbative QCD and constrain the PDFs. For example, the rapidity distributions of W and Z production constrain the mixture of sea and valence quarks. Precise experimental measurements also allow comparisons between different PDF sets and the underlying theoretical models and calculations [4]. In addition, measuring Drell-Yan lepton-pair production is very important for other LHC physics analyses since it is a major source of background for various processes, such as $t\bar{t}$ and diboson measurements, as well as for searches for new physics beyond the standard model, such as the production of high-mass dilepton resonances.

This paper presents measurements of the Drell-Yan differential cross section $d\sigma/dM$ in the dimuon and dielectron channels in the mass range $15 < M < 1500$ GeV and the double-differential cross section $d^2\sigma/dMdY$ in the dimuon channel for the mass range $20 < M < 1500$ GeV. These measurements are performed using an integrated luminosity of 4.5 fb^{-1} (dimuon) and 4.8 fb^{-1} (dielectron) of proton-proton collision data collected using the Compact Muon Solenoid (CMS) detector at the LHC at $\sqrt{s} = 7$ TeV. The differential cross section measurements are normalized to the Z-peak region (60 – 120 GeV).

This normalization cancels out the uncertainty in the integrated luminosity and reduces the PDF uncertainty in acceptance, the effect of multiple interactions per bunch crossing (pileup) in the reconstruction efficiency, and the uncertainty in the efficiency estimation. These measurements in this paper are corrected for the effects of resolution which cause event migration between bins in mass and rapidity. The observed dilepton mass is also corrected for final state radiation (FSR) due to the leptons radiating photons and changing the dilepton invariant mass. This effect is most pronounced below the Z-peak. The differential cross-sections are measured separately for both lepton flavours in the fiducial region and are extrapolated to the full phase space. The consistency of the muon and electron channels enables these to be combined and compared with the POWHEG [5] next-to-leading order (NLO) prediction and NNLO QCD predictions with FEWZ [6] using the MSTW2008 and CT10 PDFs. The $d^2\sigma/dMdY$ measurement is compared to the POWHEG next-to-leading order (NLO) prediction calculated with CT10 PDFs and the NNLO theoretical predictions as computed with FEWZ using the CT10, NNPDF2.1, MSTW2008, HERAPDF, JR09, ABKM and CT10W PDFs [7–13].

2 The CMS Detector

The central feature of the CMS detector is a superconducting solenoid providing an axial magnetic field of 3.8 T and enclosing an all-silicon inner tracker, a crystal electromagnetic calorimeter (ECAL), and a brass-scintillator hadronic calorimeter(HCAL). The tracker is composed of a pixel detector and a silicon strip tracker, that are used to measure charged-particle trajectories covering the full azimuthal angle and pseudorapidity interval $|\eta| < 2.5$. The pseudorapidity η is defined as $\eta = -\ln[\tan(\theta/2)]$, where $\cos\theta = p_z/p$. A right-handed coordinate system is used in CMS, with the origin at the nominal collision point, the x axis pointing to the center of the LHC ring, the y axis pointing up (perpendicular to the LHC plane), and the z axis along the anticlockwise-beam direction. The azimuthal angle ϕ is the angle relative to the positive x axis measured in the x-y plane. Muons are detected in the pseudorapidity range $|\eta| < 2.4$, with four stations of muon chambers. These muon stations are installed outside the solenoid and sandwiched between steel layers, which serve as both hadron absorbers and as a return yoke for the magnetic field. They are made using three technologies: drift tubes (DT), cathode strip chambers (CSC), and resistive plate chambers (RPC). The muons associated with the tracks measured in the silicon tracker have a transverse momentum (p_T) resolution of about 1-6% in the muon p_T range relevant for the analysis presented in this paper. Electrons are detected using the energy deposition in the ECAL, which consists of nearly 76 000 lead tungstate crystals that are distributed in a barrel region ($|\eta| < 1.479$) and two endcap regions ($1.479 < |\eta| < 3$). The ECAL has an ultimate energy resolution better than 0.5% for unconverted photons with transverse energies (E_T) above 100 GeV. The electron energy resolution is better than 3% for the range of energies relevant for the measurement reported in this paper. A detailed description of the CMS detector can be found elsewhere [14]. The CMS experiment uses a two-level trigger system. The L1 trigger, composed of custom hardware processors, selects events of interest using information from the calorimeters and muon detectors [15]. The High-Level Trigger (HLT) is software-based and further decreases the event collection rate by using the full event information, including that from the tracker [16].

3 Data and Monte Carlo Samples

The measurements reported in this paper are based on data recorded in 2011 with the CMS detector at the LHC at $\sqrt{s} = 7$ TeV, corresponding to an integrated luminosity of 4.5 fb^{-1} (dimuon) and 4.8 fb^{-1} (dielectron).

Monte Carlo (MC) samples are used in the analysis for determining efficiencies, acceptances, backgrounds from processes that result in two leptons, and for the determination of systematic errors. Data driven methods are also used to determine efficiency correction factors and backgrounds. MC event samples have been generated using a variety of generators at $\sqrt{s} = 7$ TeV. All MC samples are processed with the full CMS detector simulation based on GEANT4 [17] and include trigger simulation and the full chain of CMS event reconstruction.

The Drell-Yan signal samples are generated with the NLO generator POWHEG interfaced with the PYTHIA V6.4.24 [18] parton-shower generator (referred to as the POWHEG MC). Both $t\bar{t}$ and single top samples are produced with the MADGRAPH generator [19] at leading order (LO), and the tau decays were performed with TAUOLA generator [20]. The $t\bar{t}$ sample is rescaled to the NLO cross section of 157 pb. Diboson samples ($WW/WZ/ZZ$) and QCD background events are produced with PYTHIA. Inclusive single W and Z samples, both signal and background, are produced using the POWHEG MC. The proton structure is defined using the CT10 [7] parton distribution functions. All samples are generated using the PYTHIA Z2 tune [21] to model

the underlying event. Pileup effects are taken into account in MC samples which are generated with the inclusion of multiple proton-proton interactions (average of 12 interactions per bunch crossing) that have timing and multiplicity distributions similar to those expected in data. To match the observed instantaneous luminosity profile of the LHC, the simulated events are reweighted to yield the same distribution of the mean number of proton-proton interactions per bunch crossing as observed in data.

The POWHEG MC is based on NLO calculations and a correction is added to take NNLO effects into account. The NNLO effects alter the cross section as a function of the dilepton kinematic variables and are important in the low-mass region and in renormalizing the cross section. The correction is determined from the ratio between the double-differential cross sections (binned in rapidity and P_{T}) calculated at NNLO with FEWZ [6] and at NLO with the POWHEG MC. This correction factor is applied on an event-by-event basis. For a given mass range it is defined in bins of dilepton rapidity Y and dilepton transverse momentum P_{T}:

$$\omega(P_{\mathrm{T}}, Y) = \frac{(d^2\sigma/dP_{\mathrm{T}}dY)_{\mathrm{FEWZ}}}{(d^2\sigma/dP_{\mathrm{T}}dY)_{\mathrm{POWHEG}}} \tag{1}$$

The POWHEG MC events are then reweighted using the correction factor defined in Eq. 1. The reweighted signal sample is referred to as NNLO reweighted POWHEG MC and is used for all the simulation based estimations (acceptance, efficiency, FSR corrections) for both the dimuon and dielectron analyses. The differences between the NNLO reweighted POWHEG MC and the FEWZ predictions, caused by unavoidable binning/statistics constraints, are used to extract a modeling uncertainty.

4 Cross Section Measurements

This analysis measures the Drell-Yan dimuon and dielectron invariant mass spectra, $d\sigma/dM$, for the full phase space in the range 15 GeV to 1500 GeV. The absolute dimuon rapidity range covered is from 0 to 2.4 for dimuons and 0 to 2.5 for dielectrons. The double-differential cross section $d^2\sigma/dMdY$ is measured only in the dimuon channel within the detector acceptance in the range of absolute dimuon rapidity from 0 to 2.4 and dimuon invariant mass from 20 GeV to 1500 GeV.

Cross sections are calculated using the following formula

$$\sigma = \frac{N_{\mathrm{u}}}{A \cdot \epsilon \cdot \rho \cdot L_{\mathrm{int}}} \tag{2}$$

where N_{u} denotes the background-subtracted yield obtained using a matrix inversion unfolding technique to correct for the effects of the migration of events in mass due to the detector resolution . The acceptance A and the efficiency ϵ are both estimated from MC simulation, while ρ, the correction factor accounting for the differences in the efficiency between data and simulation is extracted using a data-driven technique applied to both data and simulation. Complete details of all corrections, background estimations and the effects of the detector resolution and FSR are contained in later sections of this paper. The cross sections for the measurements described are normalized to the Z-peak region ($60 < M < 120$ GeV) and thus knowledge of the integrated luminosity L_{int} is only required for the normalization (Z-peak cross section). The differential $d\sigma/dM$ cross section measurements are performed over a mass range from 15 GeV to 1500 GeV in 40 congruous mass bins.

To provide results to be used for PDF constraints, the double-differential cross section measurement is performed in dimuon rapidity Y space by choosing binning to minimize migration among rapidity bins. The mass bins for the measurement of the double-differential cross section, $d^2\sigma/dMdY$, are determined on the basis of optimization of physics backgrounds and also the number of events. The low-mass region (20 – 60 GeV), where QCD processes contribute the most and the FSR effects are significant, is divided into three bins. The Z-peak region (60 – 120 GeV) is a single bin, because in this region the Drell-Yan production is dominated by Z boson exchange, and this binning is convenient for both normalization and comparison with other measurements. The high-mass region (120 – 1500 GeV) is divided into two regions based on number of events available. The choice of binning is also chosen so that the systematic uncertainties are comparable to the statistical uncertainties away from the Z-peak region. This results in using six invariant mass bins, with bin edges: 20, 30, 45, 60, 120, 200, and 1500 GeV. For each mass bin, 24 equidistant bins of width 0.1 absolute dimuon rapidity are defined, except for the highest mass bin, where only 12 absolute dimuon rapidity bins of width 0.2 are used.

4.1 Event Selection

The experimental signature of the DY process is two isolated and oppositely charged leptons originating from the same primary vertex. The analysis presented in this paper is based on the dilepton data samples selected by a combination of inclusive double-lepton triggers.

4.1.1 Muon selection

A combination of the lowest p_{T} threshold unprescaled dimuon triggers without isolation requirement was used to select the events for the dimuon analysis. For data taken in the earlier part of 2011, the dimuon analysis is based on triggers that selected events containing at least two muons, each with a transverse momentum of above 6 GeV. For the subsequent running periods, the triggers selected events containing two muons inclusively, one with $p_{\mathrm{T}} > 13$ GeV and the other with $p_{\mathrm{T}} > 8$ GeV. The HLT matches each of the candidate muon tracks to a silicon tracker track to form an HLT muon.

Within a CSC or DT muon chamber, the hits in the multiple detection layers are fit to a straight line representing a segment of the muon track. In the offline analysis, tracks reconstructed from the hits in the silicon tracker are matched to the tracks reconstructed from the muon segments alone, and then the individual hits in the tracker and the muon detectors are refit to an overall track. In addition, to increase the acceptance for low momentum muons that may not penetrate deeply into the muon system, the tracks from the silicon tracker system are extrapolated into the muon system and the tracks that match at least one muon chamber track segment are taken to be the muon candidates. In both cases, multiple scattering and the energy loss are taken into account as the muons traverse through the CMS detector.

To select the best dimuon candidate in each event, quality control criteria are applied to the tracks. All of the muons are required to pass the standard CMS muon identification and the quality control criteria, which are based on the number of hits found in the tracker, the response of the muon chambers, and a set of matching criteria between the muon track parameters determined by the inner tracker section of the detector and as measured in the muon chambers [22]. Both muons are required to match the HLT trigger objects. Cosmic ray muons, which traverse the CMS detector close to the interaction point, can appear as back-to-back dimuons; these are removed by requiring that both muons should have an impact parameter in the transverse plane of less than 2 mm with respect to the center of the interaction region. Further, the opening angle between the two muons are required to differ from π by more than 5 mrad. In order to

reduce the fraction of the muon pairs from various light and heavy-meson decays, a common vertex for the two muons is required using a fit. The event is rejected if the dimuon vertex probability is smaller than 2%. More details on muon reconstruction and identification can be found in Ref. [22].

To suppress the background contributions from muons originating from heavy flavor quark decays and non-prompt muons from hadron decays, both muons are required to be isolated from other tracks within a cone of size $\Delta R = 0.3$, with $\Delta R = \sqrt{(\Delta\eta)^2 + (\Delta\phi)^2}$. The relative combined isolation of the muon, based on the CMS particle-flow algorithm [23], is defined as $I_{\text{rel}}^{\text{comb}} = \sum_{\Delta R<0.3}(E_{\text{T}} + p_{\text{T}})/p_{\text{T}}(\mu)$, where the sum is over the transverse energy E_{T} (as measured in the electromagnetic and hadron calorimeters) and the transverse momentum p_{T} (as measured in the tracker subsystem) of all the reconstructed neutral and charged hadrons within this cone, excluding the muon track itself. The muons are required to satisfy $I_{\text{rel}}^{\text{comb}} < 0.2$.

No attempt has been made in this analysis to use the radiated photons detected in the ECAL to correct the muon energies for possible final state radiation (FSR). See section 4.6 for a discussion of FSR effects. Each muon is required to be within the acceptance of the muon subsystem ($|\eta| < 2.4$). The leading muon in the event is required to have a transverse momentum $p_{\text{T}} > 14$ GeV and the sub-leading muon $p_{\text{T}} > 9$ GeV to avoid the trigger turn-on regime and to operate on the plateau region of the trigger efficiency. Events are selected for further analysis if they contain opposite-charge muon pairs meeting the above requirements. If more than one dimuon candidate passes these selections, the pair with the highest χ^2 probability, associated to the kinematic fit of the dimuon vertex, is retained.

4.1.2 Electron selection

The events in the dielectron channel are selected if triggered by two electrons with minimum E_{T} requirements of 17 GeV for one of the electrons and 8 GeV for the other. The selection of events at the trigger level, based on the isolation and the quality of an electron object, makes it possible for the thresholds to remain unchanged throughout the full period of 2011 data-taking in spite of rapidly increasing luminosity. The triggers for signal selection for this analysis are chosen to be the lowest unprescaled double-electron triggers. They provide the lowest E_{T} dielectrons so that one can probe the dielectron invariant mass as low as possible.

The dielectron candidates are selected online by requiring two clusters in the ECAL, each with the transverse energy E_{T} exceeding a threshold value. The offline reconstruction of the electrons starts by building superclusters in the ECAL in order to collect the energy radiated by bremsstrahlung in the tracker material. A specialized tracking algorithm is used to accommodate changes of the curvature due to the bremsstrahlung. The superclusters are then matched to the electron tracks. The electron candidates are required to have a minimum E_{T} of 10 GeV after the correction for the ECAL energy-scale. In order to avoid the inhomogeneous response at the interfaces between the ECAL barrel and endcaps, the electrons are further required to be detected within the pseudorapidity ranges $|\eta| < 1.44$ or $1.57 < |\eta| < 2.5$.

The reconstruction of an electron is based on the CMS particle-flow algorithm [23]. The electrons are identified by means of shower shape variables while the electron isolation criterion is based on a variable that combines tracker and calorimeter information. For isolation, the transverse momenta of the particles within a cone of $\Delta R < 0.3$ are summed, excluding the electron candidate itself. The ratio of the summed transverse momenta and the transverse momentum of the electron candidate ($I_{\text{PF}}/p_{\text{T}}$) is required to be less than 0.15 for all the electrons, except for those with $E_{\text{T}} < 20$ GeV in the endcaps, where the requirement is tightened to be less than 0.10. The isolation criteria were optimized to maximize the rejection of misidentified electrons from

QCD multijet production and the non-isolated electrons from the semileptonic decays of the heavy-quarks. The electron candidates are required to be consistent with a particle originating from the primary vertex in the event. The electrons originating from photon conversions are suppressed by requiring that there be no missing tracker hits before the first hit on the reconstructed track matched to the electron, and also by rejecting a candidate if it forms a pair with a nearby track that is consistent with a conversion. Additional details on electron reconstruction and identification can be found in Ref. [24].

Both electrons are selected with the impact parameter requirements $|d_{xy}| < 0.02$ cm and $|d_z| < 0.1$ cm with respect to the primary vertex. The leading electron candidate in an event is required to have a transverse momentum of $p_{\mathrm{T}} > 20$ GeV, while the trailing electron candidate must have $p_{\mathrm{T}} > 10$ GeV. Both electrons are required to match HLT trigger objects and no charge requirement is imposed on the electron pairs.

4.2 Background Estimation

There are several physical and instrumental backgrounds which contribute to the dilepton production. The main backgrounds in the region of high invariant masses (beyond the Z-peak) are due to $t\bar{t}$ and diboson production followed by leptonic decays, while the Drell-Yan production of $\tau^+\tau^-$ pairs is the dominant source of background in the region just below the Z-peak. At low values of dimuon invariant mass, most of the background events are due to QCD events with multiple jets. The situation is slightly different for electrons in the final state. At low values of dielectron invariant masses the dominant background events are from $\tau^+\tau^-$ and $t\bar{t}$ processes, whereas the contribution from QCD is small due to the stricter selection for electrons compared to muons at the trigger level.

A combination of techniques is used to determine the contributions from various background processes. Wherever feasible, the background rates are estimated from data, avoiding large uncertainties related to the simulation of these sources. The remaining contributions taken from the Monte Carlo (MC) simulation are small ($< 1\%$). The background estimation has been performed by following the same methods for both $d\sigma/dM$ and the $d^2\sigma/dMdY$ measurements.

4.2.1 Dimuon Background Estimation

In the dimuon channel, the QCD background is evaluated using a data-driven technique. This method makes use of the muon isolation and the sign of the charge as two independent discriminant variables to identify a signal region and three background regions in the two-dimensional space defined by the muon charge sign and the isolation. The background estimation is then based on the ratio between the number of signal and background events in the above regions [25].

The $t\bar{t}$ background, which is the dominant process at high-mass values, is estimated from data using a sample of events with $e\mu$ pairs. The estimated number of $\mu^+\mu^-$ can be expressed as a function of observed $e^\pm\mu^\mp$ events based on MC acceptance and efficiencies. The electron and muon candidates in the $e\mu$ sample are required to satisfy the $DY \to e^+e^-$ and $DY \to \mu^+\mu^-$ selection criteria respectively. The electron candidates are required to have $E_{\mathrm{T}} > 20$ GeV, the muon candidates $p_{\mathrm{T}} > 15$ GeV and both candidates are required to be within a range of $|\eta| < 2.4$. They are further required to pass the offline selection cuts. Whereas the $e\mu$ data sample is relatively clean, there are small backgrounds from inclusive W+jets process. The number of expected $\mu^+\mu^-$ events is calculated bin by bin as a function of invariant mass. Deviations from the MC simulation are used for assessing the systematic uncertainties. All other backgrounds are estimated using MC simulation although a data-driven estimation of all non-QCD

backgrounds has been performed with the $e\mu$ method as a cross check.

The expected shapes and relative dimuon yields from data and MC events in bins of invariant mass can be seen in Fig. 1. The expected shapes and relative dimuon yields from data and MC events in bins of dimuon rapidity, per invariant mass slice, can be seen in Fig. 2. As shown in the figure the QCD multijet process is the dominant background in the low-mass region, contributing up to about 10% in the dimuon rapidity distribution. In the high-mass regions, $t\bar{t}$ and single top production processes are dominant and collectively contribute up to about 20%.

4.2.2 Dielectron Background Estimation

In the dielectron channel, the background processes do contain true leptons in most cases. The primary contributions are due to $t\bar{t}$ and $\tau\tau$ events. The background can be divided into two categories: (1) both electrons are genuine, and (2) one or both electrons are due to misidentification.

The true electron background is estimated using the data-driven $e\mu$ method described above. The dominant electroweak background from low invariant mass up to the Z-peak is $DY \rightarrow \tau^+\tau^-$. Beyond the Z-peak the background contributions from $t\bar{t}$ and WW productions become significant, with relatively smaller contributions from the tW process. All of these processes produce $e^{\pm}\mu^{\mp}$ final state at twice the rate of the e^+e^- or $\mu^+\mu^-$. Consequently the backgrounds from these modes can be measured from a relatively clean sample of $e^{\pm}\mu^{\mp}$, after accounting for the differences in the acceptance, the efficiency and the rate. The contributions from $DY \rightarrow \tau\tau, t\bar{t}, tW$ and the dibosons to the e^+e^- spectrum are estimated from $e\mu$ data after having checked that the simulation does describe well the sample of $e\mu$ events, both in terms of the number of events as well as the shape of the invariant mass spectrum.

In addition to the real e^+e^- events from the electroweak processes there are events in which jets are falsely identified as electrons. These are either multijet events where two jets pass the electron selection criteria or W+jets events where the W decays to an electron and a neutrino pair, and the jet is misidentified as an electron. The probability for a jet to pass the requirements of the electromagnetic trigger and to be falsely reconstructed as one electron is determined from a sample of events collected with the trigger requirement for a single electromagnetic cluster to be present in the event. To ensure that this sample is dominated by jets, the events are required to have a missing transverse energy $E_{\mathrm{T}} < 10$ GeV, and events with more than one particle identified as an electron are rejected. The jet misidentification probability is measured as a function of jet E_{T} and pseudorapidity $|\eta|$. The number of e^+e^- background events is then determined from a different sample, the sample of events collected with the double electron trigger in which at least one electron candidate fails the full electron selection of the analysis. The events from this sample are assigned weights based on the expected misidentification probability for the failing electron candidates, and the sum of the weights yields the prediction for the background from this source. Since the events in this double electron trigger sample with at least one electron failing the full selection contain a small fraction of real Drell-Yan events, the contribution of the latter is subtracted using simulation.

The expected shapes and the relative yields of dielectron events from data and MC in bins of invariant mass is shown in Fig. 1, same format as the dimuon channel. The true electron background is the largest in high-mass regions due to $t\bar{t}$ events, where it reaches up to 15-20% of the observed yields. The true electron background level is also significant at $\sim$50 GeV, up to 10%, driven by $DY \rightarrow \tau^+\tau^-$ contribution. On other mass ranges the true electron background is on average several percent and particularly it is very small (less than 0.5%) under the Z-peak region. The background associated with falsely identified electrons is relatively small in the

full mass range.

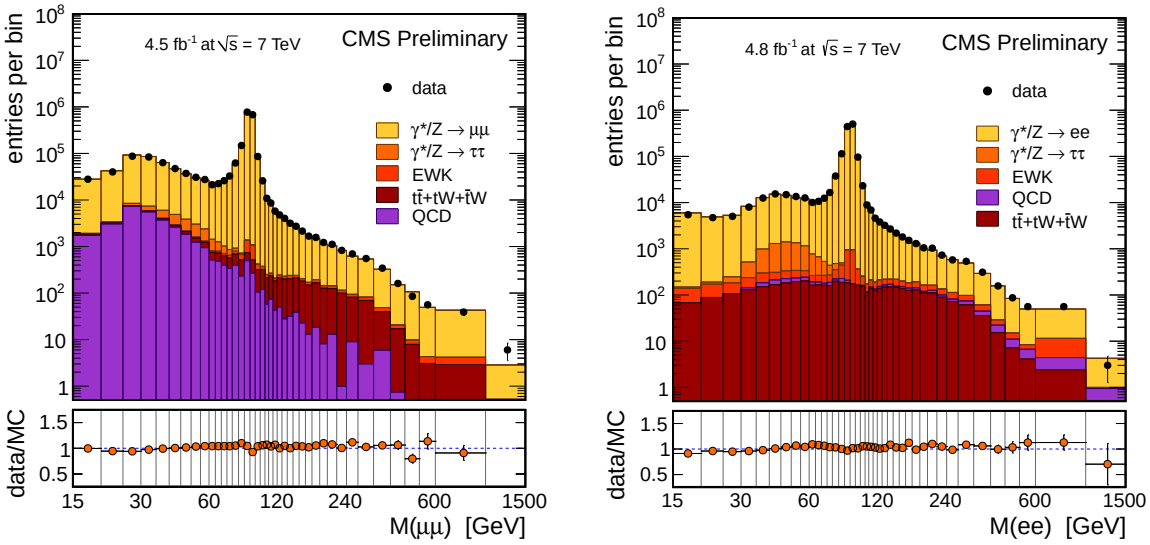

Figure 1: The observed dimuon (left) and dielectron (right) invariant mass spectra for data and MC events and the corresponding ratio of observed to expected yields. QCD and $t\bar{t}$ background yields in the muon channel and QCD in the electron channel are predicted by data-driven methods. The NNLO reweighted POWHEG MC signal sample is used. No other corrections are applied.

4.3 Energy and Momentum Resolution and Scale Corrections

The measurements of energy and momentum of each lepton directly affect the reconstructed dilepton invariant mass and are, therefore, important in obtaining a correct differential cross section.

The momentum resolution of muons below 200 GeV comes primarily from the measurements in the silicon tracker. A residual misalignment remains in the tracker that is not reproduced fully by the simulation. This misalignment leads to a bias in the reconstructed muon momenta that is removed using a momentum-scale correction.

The corrections to muon momenta are extracted separately for positive and negative muons using the average of the $1/p_{\mathrm{T}}$ spectra of muons and dimuon mass from Z decays in bins of muon charge, the polar angle θ, and the azimuthal angle ϕ. The same procedure is followed for both data and MC samples. The correction to $1/p_{\mathrm{T}}$ has two components; An additive component which removes the bias that originates from tracker misalignment; and a multiplicative component that corrects for residual mismodeling of the magnetic field. For a 40 GeV muon, the additive correction varies from 0.4 % at small η to 9 % at large η. The multiplicative correction is typically much smaller (about 0.02 %).

The average Z mass is found to be independent of ϕ. The mass of the Z-peak in the corrected distribution is different from the expected mass by only 0.10 $\pm$ 0.01% for the data and 0.00 $\pm$ 0.01% for MC. The small remaining shift in data is corrected by an additional overall scale correction. The detailed method of correction for the muon momentum is described in [26].

The energy and momentum for electrons measured with the CMS detector are derived by the measurements of the energy deposits left by the electrons in the CMS calorimeter. The energy of the deposits in the electromagnetic calorimeter is subject to a set of corrections in the stan-

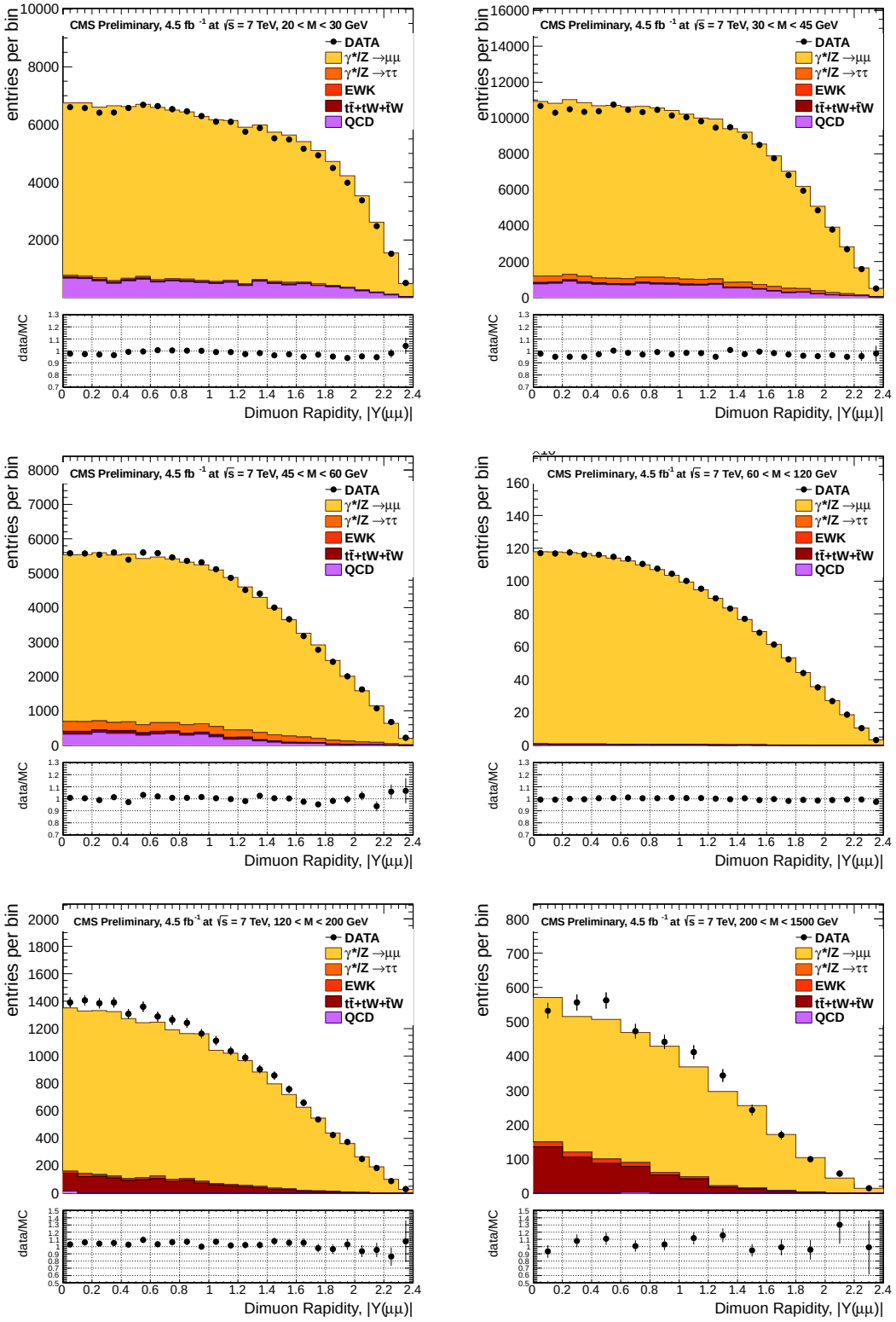

Figure 2: The observed dimuon rapidity spectra per invariant mass slice for data and Monte Carlo events. The NNLO reweighted POWHEG MC signal sample is used. The normalization factors are determined using the number of events in data in the Z-peak region, and they are applied to all of the mass slices.

dard CMS electron reconstruction procedure. Further, fine electron energy-scale corrections are obtained from the analysis of the $Z \to e^+e^-$ peak done according to the procedure described in [25]. These energy-scale corrections, which go beyond the standard CMS electron reconstruction, range from 0% to 2% depending on the pseudorapidity of the electron.

4.3.1 Unfolding

The effects of the detector resolution that result in the migration of events among analysis bins is corrected through an unfolding procedure [27]. This procedure uses the yield distribution determined from simulation by mapping it onto the measured one to obtain the true distribution. The unfolding procedure used for the differential and double-differential cross section calculations is described below.

The effect of unfolding on the differential cross section is largest in the Z-peak region (up to 30%). For the double-differential cross section measurement, the effect of unfolding is less pronounced since the invariant mass bin size is significantly wider.

The unfolding of the detector resolution effects is calculated prior to corrections for FSR. The response matrix T_{ik}, for the unfolding, which gives the fraction of events from bin i of the true distribution that ends up reconstructed in bin k, is calculated from the MC simulation:

$$N_i^{\text{obs}} = \sum_k T_{ik} N_k^{\text{true}}. \tag{3}$$

In the case of the measurement of $d\sigma/dM$, the matrix is nearly diagonal with a few significant off-diagonal elements located adjacent to the main diagonal. Both the dimuon and dielectron response matrices are invertible without regularization.

For the double-differential cross section measurement, a dedicated procedure has been developed in order to take into account the effect of migration in bins of dilepton rapidity. Within the framework of the unfolding method for the double-differential cross section measurement, a two-dimensional yield distribution (matrix) in bins of dilepton invariant mass and rapidity is transformed from a two-dimensional into a one-dimensional distribution by mapping onto a one-dimensional vector. Once the one-dimensional distribution is obtained, the unfolding procedure follows closely the standard technique for the differential $d\sigma/dM$ measurement described in [28, 29].

The unfolding response matrix T_{ik} is calculated from the Monte Carlo simulation corresponding to the one-dimensional yield vector in Eq. 3. The structure of the response matrix is quite different from the corresponding matrix derived using the yields binned in invariant mass only. The matrix consists primarily of three diagonal-dominated blocks. There are two types of off-diagonal elements in this response matrix. The elements adjacent to the diagonals originate from migration between rapidity bins within the same mass slice. Two additional sets of diagonal dominated blocks originate as a result of migration between adjacent mass slices.

The response matrix is inverted and used to unfold the one-dimensional spectrum:

$$N_k^{\text{u}} = N_k^{\text{true}} = \sum_i (T^{-1})_{ki} N_i^{\text{obs}}. \tag{4}$$

Finally, the unfolded distribution is inflated back into the two dimensional invariant mass-rapidity distribution by performing index transformation.

A set of tests was performed to validate this unfolding procedure. A closure test confirmed the validity of the procedure, which was done with the true information available in MC. The stability and the robustness of the method, with respect to statistical fluctuations in the matrix elements, was checked with an ensemble of pseudo-experiments.

4.4 Efficiency

The event efficiency ε is defined as the probability for an event within the acceptance to pass the reconstruction procedure and selection requirements. The event efficiency is obtained from MC simulation and is corrected by an efficiency scale factor $\rho_{\text{data/MC}}$ which takes into account differences between data and simulation. The determination of the event efficiency is based on the signal MC samples described in section 3. It is calculated as the ratio of the number of events that pass full reconstruction and selection to the number of events that are found within the acceptance at generator level.

The event efficiency is also significantly affected by the amount of pileup in the event. The average amount of pileup in data depends on the data-taking conditions and continued to increase throughout the data taking in 2011. To correct for this effect, pileup reweighting is performed. The pileup affects primarily the electron isolation efficiency (up to 5%) whereas the effect on the muon isolation efficiency is less than 1%. The same procedures outlined below were used to extract the data-driven efficiency corrections for both the $d\sigma/dM$ and the $d^2\sigma/dMdY$ measurements.

4.4.1 Dimuon Efficiency

The scale factor $\rho_{\text{data/MC}}$ is determined using $Z \to \mu^+\mu^-$ events from both data and MC where one muon, the tag, satisfied the tight selection requirements, and each selection criterion is applied on the other muon as a probe (tag-and-probe method [25]). To evaluate this scale factor an event sample with a single muon trigger is used where the trigger muon is the tag.

In the dimuon channel the total event selection efficiency is factorized in the following way:

$$\varepsilon = \varepsilon(\mu_1, \text{sel}) \cdot \varepsilon(\mu_2, \text{sel}) \cdot \varepsilon(\text{dimuon}, \text{sel}) \cdot \varepsilon(\text{event}, \text{trig} \,|\, \text{sel}) \tag{5}$$

- $\varepsilon(\mu, \text{sel})$ is the single muon efficiency.
- $\varepsilon(\text{dimuon}, \text{sel})$ is the efficiency that the two muon tracks of the selected dimuon event must be consistent with coming from a common vertex and satisfy the angular cut between the two muons.
- $\varepsilon(\text{event}, \text{trig} \,|\, \text{sel})$ is the efficiency of triggering an event (Level-1 and HLT). It includes the efficiency that an identified muon is matched to a trigger object.

The single muon efficiency is factorized into the following three conditional terms:

$$\varepsilon(\mu, \text{sel}) = \varepsilon(\text{track} \,|\, \text{acc}) \cdot \varepsilon(\text{reco} + \text{id} \,|\, \text{track}) \cdot \varepsilon(\text{iso} \,|\, \text{reco} + \text{id}) \tag{6}$$

- $\varepsilon(\text{track} \,|\, \text{acc})$ is the offline track reconstruction efficiency, i.e. the efficiency that a muon track is accepted (identified) in the tracker.
- $\varepsilon(\text{reco} + \text{id} \,|\, \text{track})$ is the muon reconstruction and identification efficiency, i.e. the efficiency that the reconstructed muon passes all the offline quality cuts.
- $\varepsilon(\text{iso} \,|\, \text{reco} + \text{id})$ is the muon isolation efficiency.

The double muon trigger has asymmetric p_T selections for each leg and, therefore, the efficiency for a muon to trigger the high p_T leg (leg 1) is different than the efficiency for a muon to trigger the low p_T leg (leg 2). We define one leg efficiencies where $\varepsilon(\mu, \text{trig1} \,|\, \text{sel})$ is the efficiency of an offline selected muon to be matched to one leg of the double muon trigger, and $\varepsilon(\mu, \text{trig2} \,|\, \text{sel})$ is the efficiency of an offline selected muon to be matched to the other leg of the double muon trigger. For a double muon trigger with asymmetric thresholds, $\varepsilon(\mu, \text{trig1} \,|\, \text{sel}) \neq \varepsilon(\mu, \text{trig2} \,|\, \text{sel})$. The efficiency factor $\varepsilon(\mu, \text{trig1} \,|\, \text{sel})$ corresponds to a muon matched to the leg of the double muon trigger that has the higher p_T threshold. The double muon trigger efficiency can then be factorized with single muon trigger efficiencies in the following way which takes into account the different efficiencies for two legs:

$$\begin{aligned}\varepsilon(\text{event}, \text{trig} \,|\, \text{sel}) = {} & \varepsilon(\mu_1, \text{trig1} \,|\, \text{sel}) \cdot \varepsilon(\mu_2, \text{trig2} \,|\, \text{sel}) + \varepsilon(\mu_1, \text{trig2} \,|\, \text{sel}) \cdot \varepsilon(\mu_2, \text{trig1} \,|\, \text{sel}) \\ & - \varepsilon(\mu_1, \text{trig1} \,|\, \text{sel}) \cdot \varepsilon(\mu_2, \text{trig1} \,|\, \text{sel}).\end{aligned} \tag{7}$$

The above efficiencies for muon reconstruction, identification, isolation and trigger efficiencies are obtained from identical analyses of $Z \to \mu^+\mu^-$ data and MC samples where one muon satisfied the tight selection requirements and the required selection was probed on the other muon. For these measurements the combinatorial background of tag-probe pairs not coming from the Z were subtracted using a simultaneous maximum likelihood fit to the invariant mass spectra for passing and failing probes with identical signal shape and background shapes.

Finally, the efficiency scale factor $\rho_{\text{data/MC}}$ was determined and event efficiencies as a function of mass, rapidity and p_T were calculated. The scale factor is $1.02 - 1.03$ rising to 1.10 at high rapidity.

4.4.2 Dielectron Efficiency

The factorization of the event efficiency for the electron channel and for the dielectron channel analysis is similar to that of the dimuon analysis. The total event selection efficiency is given by:

$$\varepsilon = \varepsilon(e_1, \text{sel}) \cdot \varepsilon(e_2, \text{sel}) \cdot \varepsilon(\text{event}, \text{trig} \,|\, \text{sel}) \tag{8}$$

where the two $\varepsilon(e, \text{sel})$ terms are the single electron efficiencies for the two electrons in the candidate and $\varepsilon(\text{event}, \text{trig} \,|\, \text{sel})$ is the efficiency of triggering on the event. There is no term $\varepsilon(\text{dielectron}, \text{sel})$ analogous to the one in Eq. 5 because there is no requirement in the selection for dielectron candidates that depends on parameters of both electrons at the same time except for the requirement to originate from the common vertex. This factor, however, is absorbed into the single electron efficiency by requiring for each of the electrons a small enough impact parameter with respect to the primary vertex of the event.

The single electron efficiency is factorized as

$$\varepsilon(e, \text{sel}) = \varepsilon(\text{reco} \,|\, \text{SC}) \cdot \varepsilon(\text{id} + \text{iso} \,|\, \text{reco}) \tag{9}$$

- the efficiency to detect a supercluster (SC) is known to be very close to 100%.
- $\varepsilon(\text{reco} \,|\, \text{SC})$ is the offline electron reconstruction efficiency, i.e. the probability that, given a SC, an electron can be reconstructed and found to be a 'good' electron with the offline selection.

- $\varepsilon(\text{id} + \text{iso} \,|\, \text{reco})$ – the efficiency to pass the selection criteria specific to this measurement, including identification, isolation, and conversion rejection, given that the electron candidate has already passed the previous stage of the offline selection.

The efficiency for an event to pass the trigger is computed in the following way:

$$\varepsilon(\text{event}, \text{trig} \,|\, \text{sel}) = \varepsilon(e_1, (\text{trig1.OR.trig2}) \,|\, \text{sel}) \cdot \varepsilon(e_2, (\text{trig1.OR.trig2}) \,|\, \text{sel}) \tag{10}$$

where $\varepsilon(e_i, (\text{trig1.OR.trig2}) \,|\, \text{sel})$ is the efficiency for each electron to match either one of the two trigger legs. This factorization is more simple than that of muons given by Eq. 7 because for the dielectron trigger it has been measured that $\varepsilon(e, \text{trig1} \,|\, \text{sel}) \approx \varepsilon(e, \text{trig2} \,|\, \text{sel})$, in which case Eq. 7 simplifies to Eq. 10.

For the electron channel, the efficiencies for electron reconstruction, selection, and the trigger efficiencies are obtained from $Z \to e^+e^-$ data samples following the same tag-and-probe method discussed above for the muons.

4.5 Acceptance

The geometrical and kinematic acceptance A is defined as the fraction of events within the detector fiducial volume. The detector fiducial volume is defined by the nominal p_{T} and η requirements for an analysis using the simulated leptons after the FSR simulation. It is determined from simulation using the NNLO reweighted POWHEG MC.

The correction to pre-FSR quantities (generator level Z/γ^* mass) is important since the theoretical calculations may not include FSR. The conversion depends on the exact FSR model in MC and this is addressed in the next sections.

The signal event selection efficiency ϵ per mass bin is the fraction of events inside the acceptance that pass the full selection. Note that this definition uses the same generator level post-FSR quantities in both the numerator and denominator (as in the acceptance definition). The following equation holds:

$$A \cdot \epsilon \equiv \frac{N^A}{N^{\text{GEN}}} \cdot \frac{N^\epsilon}{N^A} = \frac{N^\epsilon}{N^{\text{GEN}}} \tag{11}$$

where N^{GEN} is the full number of generated signal events in a given invariant mass bin, N^A are the events inside the geometrical and kinematic acceptance and N^ϵ is the number of events passing the analysis selection. The efficiency is estimated using the NNLO reweighted POWHEG MC and data-driven corrections are applied as described in section 4.4.

The acceptance calculation depends on higher order QCD corrections and the choice of PDFs. The use of an NNLO signal MC is essential, especially in the low-mass region where the NLO to NNLO corrections are sizable.

The acceptance calculation for the $d^2\sigma/dMdY$ double-differential cross section measurement is highly model dependent. Therefore, the double-differential cross section is measured within the detector acceptance, and only the efficiency correction is applied.

Fig. 3 shows the acceptance, the event efficiency and $A \times \epsilon$ as functions of the dilepton invariant mass.

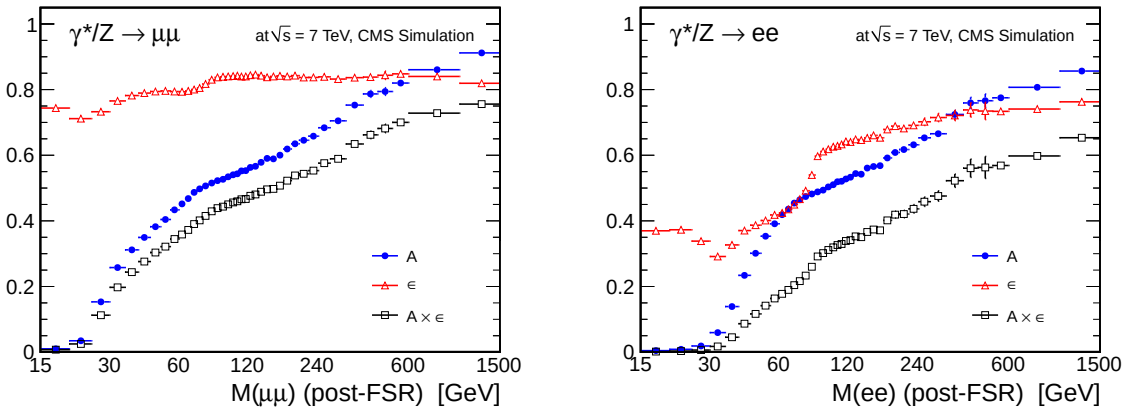

Figure 3: The Drell-Yan acceptance, efficiency and their product per invariant mass bin in the dimuon channel (left) and the dielectron channel (right).

4.6 Final State QED Radiation Effects

Leptons can radiate predominantly collinear photons in a process referred to as FSR. This FSR effect changes the observed invariant mass, which is computed from the 4-momenta of the two leptons. When FSR photons with sizable energy are emitted, the observed mass can be substantially lower than the propagator in the hard interaction. The effect is most pronounced just below the Z-peak, where the 'radiative' events in the Z-peak are shifted lower in mass and become a significant contribution to that mass region.

The correction for FSR effects is performed separately from the correction for detector resolution effects. The FSR correction procedure is performed in three steps:

1. A bin-by-bin correction for the events in which pre-FSR leptons fail the acceptance cuts while post-FSR leptons pass. At the analysis level we deal only with post-FSR events and this correction, based on MC results, scales back the sample to contain only events that pass acceptance cuts in both pre- and post-FSR. The correction is applied before the next step, FSR unfolding, and is somewhat similar in meaning to a background correction.

2. An unfolding procedure is used for the events in which both pre-FSR and post-FSR leptons pass the acceptance cuts, for which we can construct a response matrix similar to Eq. 4. The resulting invariant mass and rapidity at the pre-FSR or post-FSR level may or may not be in the range of interest, and if not, the event is properly taken care of by the underflow and overflow bins.

3. A bin-by-bin correction is used for the events in which pre-FSR leptons pass the acceptance cuts, but post-FSR leptons fail those cuts. These events do not enter the response matrix, but they need to be taken into account. This correction is applied after the FSR unfolding, and is similar to an efficiency correction.

The correction for the events from step 1 is quite small, reaching its maximum of 1% right below the Z-peak.

The unfolding procedure for the events from step 2 follows the unfolding procedure for the resolution. The response matrix is derived from the NNLO reweighted POWHEG MC sample, using pre-FSR and post-FSR yields.

Finally, the bin-by-bin correction for the events from step 3 is significant at low-mass reaching a maximum of 20% in the lowest mass bin and decreasing to negligible levels in the Z-peak region.

The same method is applied to the double differential measurement. The structure of the response matrix is quite different from the corresponding matrix derived using the yields binned in invariant mass only. The matrix consists of a set of diagonal-dominated blocks which originate from migration between mass slices in the pre- and post-FSR distributions.

4.7 Systematic Uncertainties

Systematic uncertainties have been evaluated for each analysis step in the differential and the double-differential cross section calculations. The methods to evaluate the uncertainties are described in [28].

4.7.1 Dimuon Systematic Uncertainties

In the muon channel, the dominant systematic uncertainty comes from the efficiency correction containing two factors: the event efficiency ε measured from signal MC, and the efficiency scale factor $\rho_{\mathrm{data/MC}}$ that reflects systematic deviations between data and simulation. The uncertainty on ϵ, related to the size of the signal MC sample, is negligibly small, while the uncertainty on $\rho_{\mathrm{data/MC}}$ is significant (up to 2%). As discussed in Section 4.4, single muon efficiencies of several types are measured with the tag-and-probe procedure and are combined into event level efficiency scale factors. The tag-and-probe procedure yields the efficiency of each kind with a certain statistical error. A variety of possible systematic biases in the tag-and-probe procedure have been investigated, such as dependence on binning in single muon p_T and η, dependence on the assumed shape of signal and background in the fit model, and others. Appropriate systematic errors on the single electron efficiency scale factors have been assigned. The effect of the combined statistical and systematic uncertainties of the event level scale factors $\rho_{\mathrm{data/MC}}$ on the final result constitutes the final systematic error from this source. This error is evaluated by recomputing the final result multiple times using an ensemble of the single muon efficiency maps where the entries are randomized within $\pm 1 \cdot \sigma$ of the combined statistical and systematic errors on the map bins.

The methods to evaluate the background systematic uncertainty are different for MC-based and data-driven approaches. The data-driven method is used to estimate the QCD, $t\bar{t}$, and single top quark backgrounds whereas all the other backgrounds are evaluated from simulation. With the data-driven technique, we assign the systematic uncertainty based on two sources: the Poissonian statistical uncertainty of predicted backgrounds (which is treated as systematic), and the deviation of the data-driven prediction from the arithmetic mean of the data-driven prediction and corresponding MC expectation. The resulting uncertainty is a combination of these two sources in quadrature. In the case of a MC-based estimation, the systematic uncertainty in the background estimation consists of two components: Poissonian statistical uncertainty from the MC sample (which is treated as systematic), and systematic uncertainty due to the knowledge of the theoretical cross section. These two components are combined in quadrature.

In the muon momentum-scale correction, the efficiency estimation, the background subtraction, the detector resolution effect, the modeling of the Z boson p_{T} spectrum, and the modeling of the FSR of the photon are considered as sources of systematic uncertainty. To assign the systematic error of the muon momentum-scale correction in the measurement, the muon momentum-scale correction is shifted by one sigma of the total error of the muon momentum-scale correction and the deviation of the differential cross section from the central value is as-

signed as the systematic error. This uncertainty is used to estimate the systematic uncertainty of the detector resolution by the unfolding method.

The systematic uncertainty due to the model dependent FSR simulation in the dimuon channel is estimated using two reweighting techniques on the signal MC events. One is the electroweak radiative correction [30]. This correction is applied to the electromagnetic coupling constant and the difference in total event counts between reweighted and original events is assigned as a systematic uncertainty. The second uses photons reconstructed near a muon. In this case, the additional scale factors are determined by comparing data and MC using three distributions: the number of photons, photon energy, and $\Delta R(\mu, \gamma)$. These factors are consequently applied to the signal MC events. The effect from the photons is non-negligible in the low-mass region ($M < 45$ GeV) where a large contribution from fake photons creates an additional systematic uncertainty.

We assign a systematic uncertainty in the unfolding of detector resolution effects from two sources; (1) 1.5% error from the momentum-scale correction, which is determined as a difference between the central value of the unfolded distribution and the shifted value of the unfolded distribution; and (2) 0.5% error in the momentum-scale correction estimation method. We assign a systematic error due to unfolding, which also consists of two sources; (1) 1% error due to the systematic difference in data and MC distributions (which must be taken into account, as the response matrix is determined fully from MC), and (2) up to 1% uncertainty in the unfolding method. To estimate the uncertainty due to the systematic difference in data and MC distributions, a bias in unfolding is simulated by using the migration matrix from MC in bins of the true mass and measured mass, generating ensembles of pseudo-experiments of true and measured data while holding the response matrix fixed. Each ensemble is obtained by smearing the initial observed yield vector with a random Gaussian distribution (taking the width of the Gaussian equal to 1% of the yield value in a given bin and this provides sufficient variation within the detector resolution). These ensembles of pseudo-experiments are unfolded and the pull of each ensemble is taken. The mean of the pulls over the set of ensembles is calculated, and the corresponding systematic uncertainty is assigned as:

$$\frac{\delta N^{\mathrm{obs}}|_{syst}}{N_{\mathrm{u}}} = \mu_{\mathrm{pulls}} \cdot \frac{\delta N^{\mathrm{obs}}|_{stat}}{N_{\mathrm{u}}} \tag{12}$$

The systematic effect of the unfolding is small (less than 1%) except in the highest-populated bins.

The acceptance-efficiency uncertainty is considered because it dominates at low mass. It contains an error related to the statistics of the MC sample that limits our knowledge of the $A \times \epsilon$ which we treat as systematic. The corresponding error is a Clopper-Pearson interval for the ratios of Poisson means. The acceptance calculation is highly model dependent. There is an uncertainty due to imperfect knowledge of the PDFs, describing the soft part of the collision, and the modeling of the hard interaction process (namely, the effects of higher order QCD corrections). These contributions are largest at low-mass regions (10%) and decrease to less than 1% for masses above the Z-peak. The effects of higher order EWK corrections in comparison to the FSR corrections are small. They increase for invariant masses in the TeV region, but are insignificant compared to our experimental precision for the whole mass range under study.

The PDF uncertainties for the differential and double-differential cross section measurements are calculated using the LHAGLUE interface to the PDFs library LHAPDF [31, 32], by applying a reweighting technique with asymmetric errors as described in [33]. The PDF uncertainty in the acceptance, i.e. the modeling uncertainty, is not considered as a part of the resulting

uncertainty in the measurement, but is rather used to facilitate comparison with theoretical models.

4.7.2 Dielectron Systematic Uncertainties

In the electron channel, the leading systematic uncertainty is associated with the energy scale corrections of individual electrons. The corrections affect both the placement of a given candidate in a particular invariant mass bin and the likelihood of surviving the kinematic selection. The energy scale correction itself is calibrated to 1-2% precision. Several sources of systematic uncertainties due to the energy scale correction are considered: (1) the corrective factors are determined with certain precision; (2) the residual differences in simulated and measured distributions; (3) the choice of line shape modeling; and (4) the choice of η binning. The associated error in the signal yield is calculated by varying the energy scale correction value within its error amount and remeasuring the yield. Electron energy scale uncertainty takes its largest values for the bins near the central Z-peak bin because of sizable event migration. This uncertainty for the electron channel is of the order of 20 times larger than the momentum scale uncertainty for muons, for which the associated systematic uncertainties in the cross section are rather small.

Another significant uncertainty for electrons results from the uncertainty in the efficiency scale factors. The systematic uncertainty in the scale factors as well as the resulting error on the normalized cross section are found with the same procedure as for the muon channel.

The dielectron background uncertainties are evaluated by comparing the background yields calculated as described in Section 4.2 with predictions from simulation. These uncertainties become dominant at the higher invariant masses above the Z-peak. The uncertainty associated with the unfolding procedure in the electron channel comes primarily from the uncertainty in unfolding the matrix elements due to imperfect simulation of detector resolution. This simulation uncertainty for electrons is significantly larger than for muons, leading to a larger systematic uncertainty in the normalized cross section. The uncertainties due to FSR effects are estimated with a method similar to that for the muon channel discussed above with similar values. Because of significantly higher systematic uncertainty from other sources for all mass bins for the electron channel than for the muon channel, the FSR related contribution to the electron channel systematic uncertainty is neglected. The PDF uncertainties affecting the acceptance have been computed the same way as described for the muon channel.

The systematic effects due to FSR simulation uncertainty for the electron channel primarily affect the detector resolution unfolding procedure. The impact of these effects is higher for the electron channel in comparison to that for the muon channel because of the FSR photon recovery in the CMS electron reconstruction procedure as well as because of the overall stronger FSR effects for the electron channel. Differently from the described procedure for the muon channel, a more conservative approach is adopted here: the final results of the measurement are recomputed using the detector resolution unfolding matrix prepared with varying the fraction of events with significant FSR ($>1\,\text{GeV}$) in simulation by $\pm 5\%$, and taking the spread as the systematic error. This systematic error is absorbed into the total detector resolution unfolding systematics. The effect of the FSR simulation on other analysis steps for the electron channel is negligible in comparison to other systematic effects associated with those steps.

If an uncertainty on the centre-of-mass energy of 100 GeV is assumed this would result in an additional uncertainty in the differential cross section of 0.5% in the low-mass region, 1.4% in the Z-peak region and 2% in the high-mass region on the average.

5 Results and Discussion

This section provides a summary of the results for the $d\sigma/dM$ cross section measurements in the dielectron and dimuon channels and the $d^2\sigma/dMdY$ cross section measurement in the dimuon channel.

5.1 $d\sigma/dM$ differential cross section measurement

In order to reduce systematic uncertainties, the Drell-Yan $d\sigma/dM$ differential cross section is normalized to the cross section in the Z-peak region ($60 < M < 120$ GeV). The result of the measurement is calculated as the ratio:

$$R^i_{\text{pre FSR}} = \frac{N^i_{\text{u}}}{A^i \epsilon^i \rho^i} \Big/ \frac{N^{\text{norm}}_{\text{u}}}{A^{\text{norm}} \epsilon^{\text{norm}} \rho^{\text{norm}}} \tag{13}$$

where N^i_{u} is the number of events after the background subtraction and unfolding procedure for the detector resolution and FSR correction, the acceptances A^i, the efficiencies ϵ^i, and the corrections estimated from data ρ^i, in a given invariant mass bin i are defined earlier in the text. For both lepton channels the cross sections in the Z-peak measured in this analysis are in a very good agreement with the previous CMS measurement [25]. The results are normalized to the invariant mass bin widths, ΔM^i, defining shape $r^i = R^i/\Delta M^i$.

The results of the Drell-Yan cross section measurement are presented in Fig. 4 for both the muon and the electron channels. The muon and electron cross sections in the Z-peak are in good agreement with NNLO theory predictions (e.g. the NNLO prediction is 970 ± 30 pb [25]).

The theoretical predictions include leptonic decays of Z bosons with full spin correlations as well as the $\gamma^* - Z$ interference effects. The effects of lepton-pair production in $\gamma\gamma$ initiated processes, where both initial state protons radiate a photon, are calculated with FEWZ 3.1.b2 [35]. They are important for the high-mass region particularly and are included as additional systematic uncertainties to our theory prediction, which take into account the difference between NLO and LO on the EWK correction. The effect rises to approximately 10% in the highest mass bins. The uncertainties in the theoretical predictions due to the imprecise knowledge of the PDFs are calculated with the LHAGLUE interface to the PDF library LHAPDF, using a reweighting technique with asymmetric uncertainties. Since this is a shape measurement, and the normalization of the spectrum is defined by the number of events in the Z-region, the uncertainty is calculated for the ratio of yields between each mass bin and the Z-peak.

As seen, the result of the measurement is in good agreement with the NNLO theoretical predictions (CT10) as computed with FEWZ 2.1.1. The error band in Fig. 4 for the theory calculation includes the statistical error from the FEWZ calculation and 68% CL PDF uncertainty combined in quadrature (blue band). The effect of the higher order EWK correction computed with FEWZ 3.1.b2, as described above is included as an additional systematic uncertainty (green band). Differences between NLO and NNLO values in theory expectations are significant in the low-mass region, as reported in [28]. Therefore, this measurement is sensitive to NNLO effects. However, this measurement does not provide sufficient sensitivity to distinguish between different PDFs. Instead, the double-differential cross section measurement is necessary to provide sufficient sensitivity for the PDF constraints.

The measurements in the two channels are combined using the procedure defined in Ref. [36], which provides a full covariance matrix for the uncertainties. Given the cross section measurements in the dimuon and dielectron channels, and their symmetric and positive definite

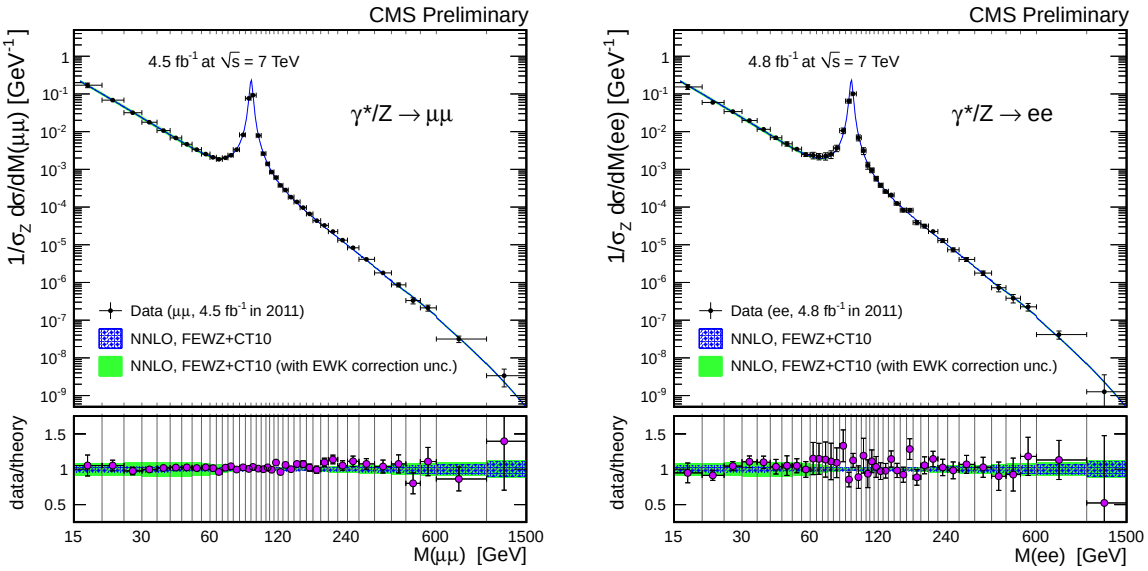

Figure 4: The Drell-Yan dimuon and dielectron invariant mass spectra, normalized to the Z-peak region, $r = (1/\sigma_Z\, d\sigma/dM)$, as measured and as predicted by FEWZ+CT10 NNLO calculations, for the full phase space. The vertical error bar for the measurement indicates the experimental (statistical and systematic) uncertainties summed in quadrature with the theory uncertainty resulting from the model-dependent kinematic distributions inside each bin. The blue error band for the theory calculation includes the statistical error from the FEWZ calculation and 68% confidence limit (CL) PDF uncertainty combined in quadrature. The uncertainty of EWK correction including $\gamma\gamma$ initiated processes effect is added in the green error band. The data point abscissas are according to Ref. [34].

covariance matrices, the estimates of the true cross section values are found as unbiased linear combinations of the input measurements having a minimum variance.

The uncertainties are considered to be uncorrelated between the two analyses. Exceptions are the modeling uncertainty which is 100% correlated between channels and the uncertainty in the acceptance which is driven mainly by the PDFs. The acceptance is almost identical between the two channels and differences in uncertainties between them are negligible. Thus when combining the measurements we add the uncertainty in the acceptance (in quadrature) to the total one after the combination is done. The acceptance uncertainty is considered diagonal so there is no attempt to include correlations on analysis bins from the PDFs since they are constrained by the measurement.

Fig. 5 shows the Drell-Yan cross section measurement in dimuon and dielectron channels combined normalized to the Z-peak region with the FSR effect taken into account.

5.2 $d^2\sigma/dMdY$ double-differential cross section measurement

The result of the double-differential cross section measurement is presented as the following ratio

$$R^{ij}_{\text{pre FSR, DET}} = \frac{N^{ij}_{\text{u}}}{\epsilon^{ij}\rho^{ij}} \Big/ \frac{N^{\text{norm}}_{\text{u}}}{\epsilon^{\text{norm}}\rho^{\text{norm}}}. \tag{14}$$

The quantities N^{ij}_{u}, ϵ^{ij}, ρ^{ij} are defined in a given bin $(i,\ j)$, with i corresponding to the binning

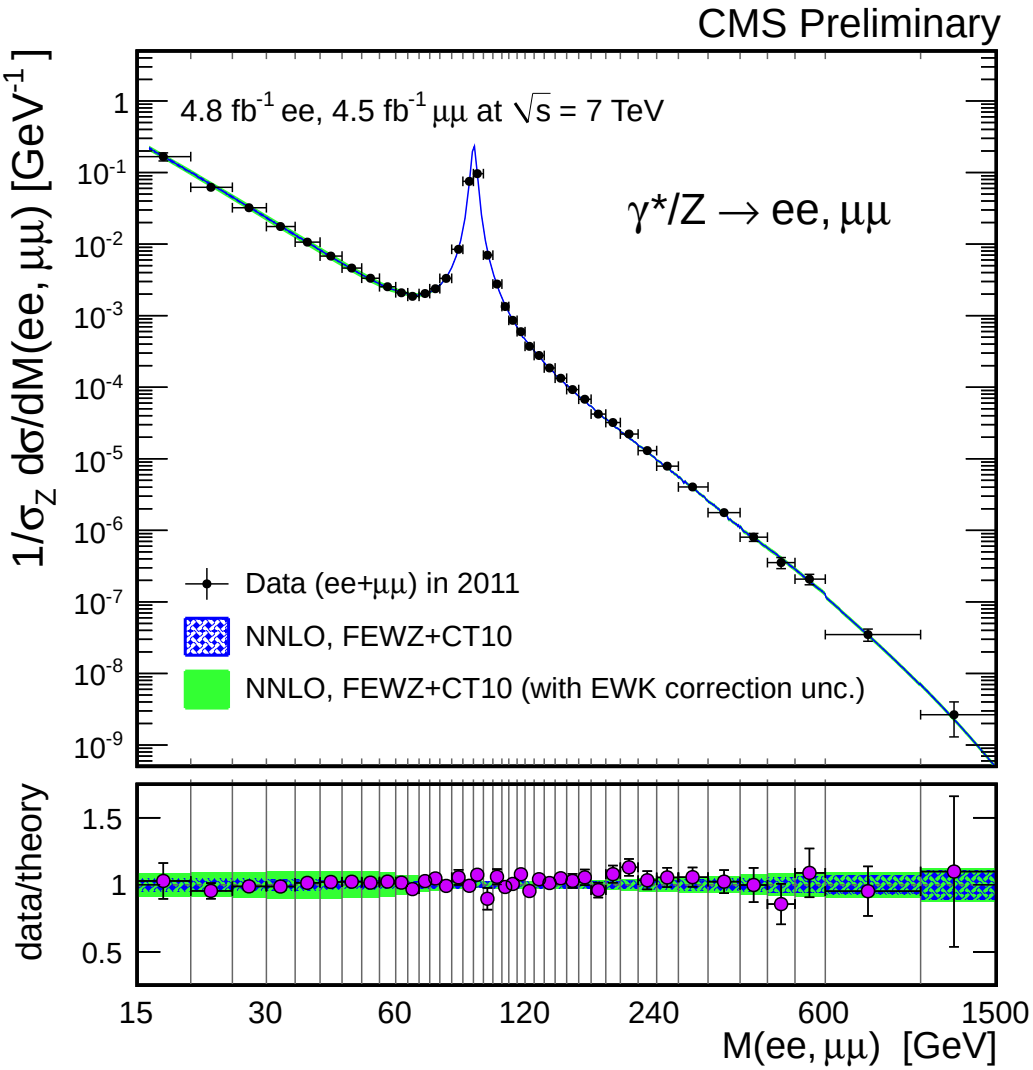

Figure 5: Combined Drell-Yan differential cross section measurement in dimuon and dielectron channels normalized to the Z-peak region with the FSR effect taken into account. Including the correlations between the two channels, the normalized χ^2 calculated with total uncertainties on the combined results is 1.1 between data and theory expectation.

in invariant mass, and j corresponding to the binning in absolute rapidity. The N_u^{norm}, ϵ^{norm}, and ρ^{norm} refer to the Z-peak region within $|Y| < 2.4$. The normalization factors between data and theory predictions are in good agreement within the error. The results are normalized to the dimuon absolute rapidity bin widths, ΔY^j, defining shape $r^{ij} = R^{ij}/(\Delta Y^j)$. The full phase space correction does not help to increase the sensitivity of PDF constraints. Therefore this measurement is performed within the detector acceptance in order to reduce the model dependence. We use the NNLO reweighted POWHEG sample in this measurement, which is discussed in section 3. This sample is used to derive the selection efficiency and produce response matrices for detector resolution and FSR corrections.

Fig. 6 shows the results for the double-differential cross section. The results are compared to NLO FEWZ+CT10 PDF and NNLO FEWZ+CT10 PDF theoretical calculations. The results of the measurement are in better agreement with NNLO CT10 predictions than with NLO CT10.The CT10 PDF set is a general-purpose NLO PDF set with 52 eigenvectors and uses a variable strong

coupling $\alpha_s(M_Z)$ in the range $0.116 - 0.120$ and $0.112 - 0.127$. The CT10 (NNLO) is also a general purpose PDF set. It includes a part of the data sample for DØ Run-2 W charge asymmetry [37] that is not included in the CT10 NLO fit. The W charge asymmetry data primarily modifies the slope of the ratio $d(x, Q^2)/u(x, Q^2)$ at large x. The CT10 (NNLO) PDF set uses a variable strong coupling $\alpha_s(M_Z)$ in the range of $0.116 - 0.120$ and $0.110 - 0.130$. We have chosen CT10 (NLO) and CT10 (NNLO) to compare with our measurement in Fig. 6 because we have used the CT10 (NLO) for the POWHEG MC signal sample. The error bands in the theory expectations include the statistical error and the PDF error from the FEWZ calculations summed in quadrature (shade). The statistical error (solid color) is relatively smaller than the PDF error and the latter is the dominant uncertainty in the FEWZ calculations. In general, the PDF error assignment is different for each PDF set. For instance, CT10 (NLO) and CT10 (NNLO) PDF errors correspond to a 90% CL, however, to get a consistent comparison with other PDF sets, the errors were scaled to the 68% CL errors.

In the low-mass region and the Z-peak region, we observe good agreement between data and theory. The NNLO effects are more significant in the low-mass region. The corrections for the $\gamma\gamma$ initiated processes calculated with FEWZ 3.1.b2 are negligible in the double-differential cross section measurement because the effects are approxmiately constant for the rapidity dependence and they are canceled out by the normalization to the Z-peak cross section.

In order to assess the sensitivity of the double-differential cross section measurement to the PDF uncertainties, we perform a comparison with the theory expectations calculated with various PDF sets. Fig. 7 shows the comparison with currently available NNLO PDFs, most of which are from the pre-LHC era: CT10, CT10W, NNPDF2.1, HERAPDF, MSTW2008, JR09 and ABKM.

The PDFs of the pre-LHC era were significantly constrained by deep inelastic scattering (DIS), inclusive jet, ν-nucleon, Drell-Yan and W charge asymmetry data from H1-ZEUS [38], SLAC [39], FNAL E665, E772, E866 [40, 41] and later CDF and DØ [37] experiments. The DIS experimental data provided important constraints on the quark and antiquark distributions, as well as the gluon distributions at medium and small x. Drell-Yan data from the fixed target experiments helped improve the understanding of the antiquark contributions. On the other hand, the collider vector boson production data helps in constraining the u/d ratio at high x and the valence quark distributions. The collider inclusive jet data covered a wide range in x and Q^2 and was particularly important in constraining the high x gluon distribution. The experiments mentioned above covered a broad range of dilepton invariant mass and Bjorken x: $M \leq 20$ GeV and $x > 0.01$.

As seen in Fig. 7, the predictions of various existing PDF sets are rather different, especially in the low-mass region, high-mass and high-rapidity regions. Given the uncertainties, the measurement presented provides sufficient sensitivity to different PDFs and can be used for a new generation of PDFs. The error bands in the theory expectations in the figure indicate the statistical error from the FEWZ calculation.

At low-mass ($20 - 45$ GeV), we observe that the values of the double-differential cross section calculated with NNPDF2.1 are higher than other PDFs. The NNPDF2.1 calculation shows good agreement with the measurement result in the $20 - 30$ GeV region, but it deviates from the measurement in the $30 - 45$ GeV region by about 10%. In the peak region, all predictions are relatively close to each other and agree well with the measurements. At high-mass the JR09 PDF calculation predicts significantly larger values compared to other PDF sets. The statistical errors of the measurements are of the order of the theoretical predictions spread for $M > 200$ GeV.

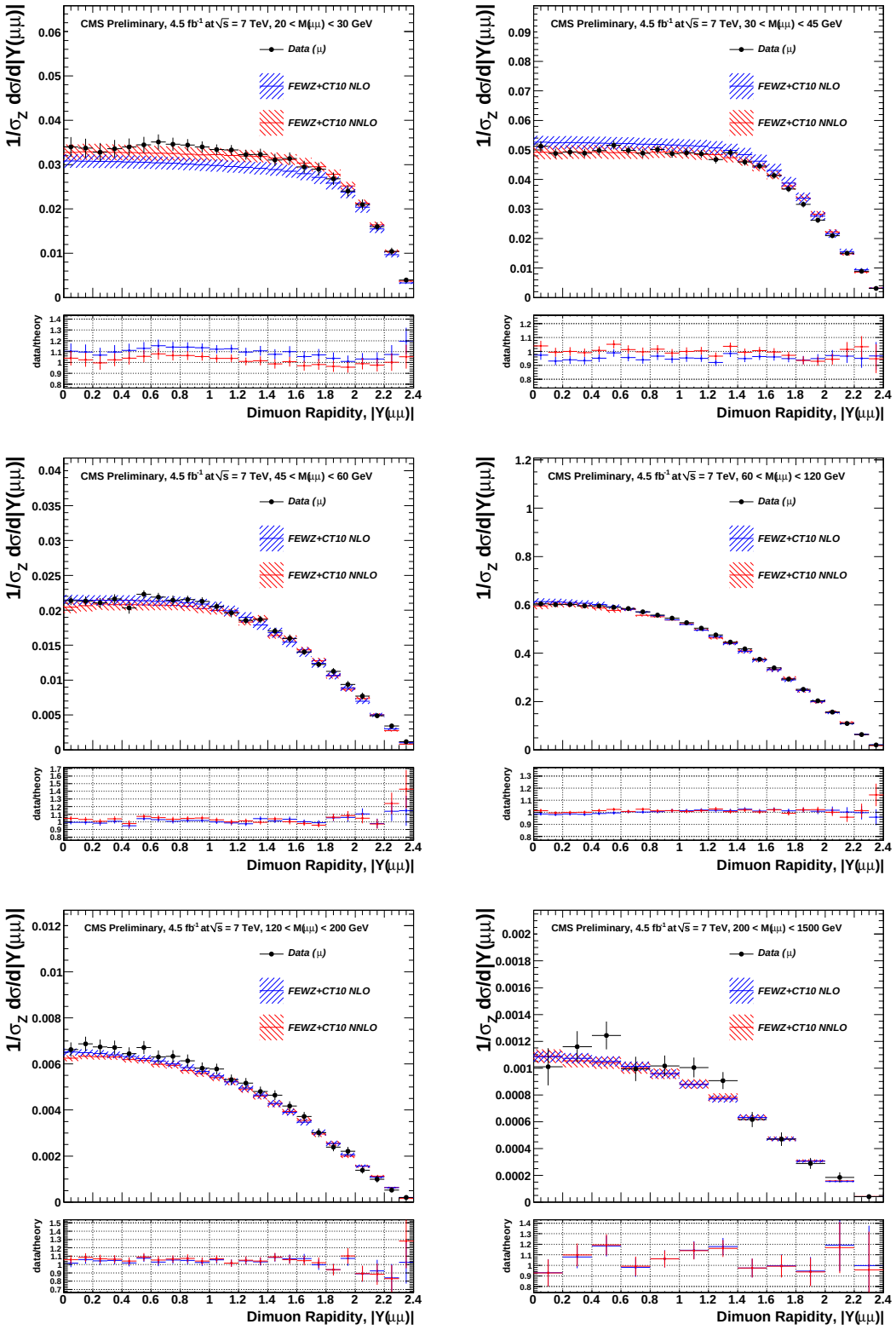

Figure 6: The Drell-Yan rapidity spectrum, plotted for different mass regions within the detector acceptance, normalized to the Z-peak region, $r = (1/\sigma_{ll} d^2\sigma/d|Y|)$, as measured and as predicted by NLO FEWZ+CT10 PDF and NNLO FEWZ+CT10 PDF calculations. The error bands in the theory predictions combine the statistical calculation error and the PDF error (shade). The solid color indicates statistical calculation error only.

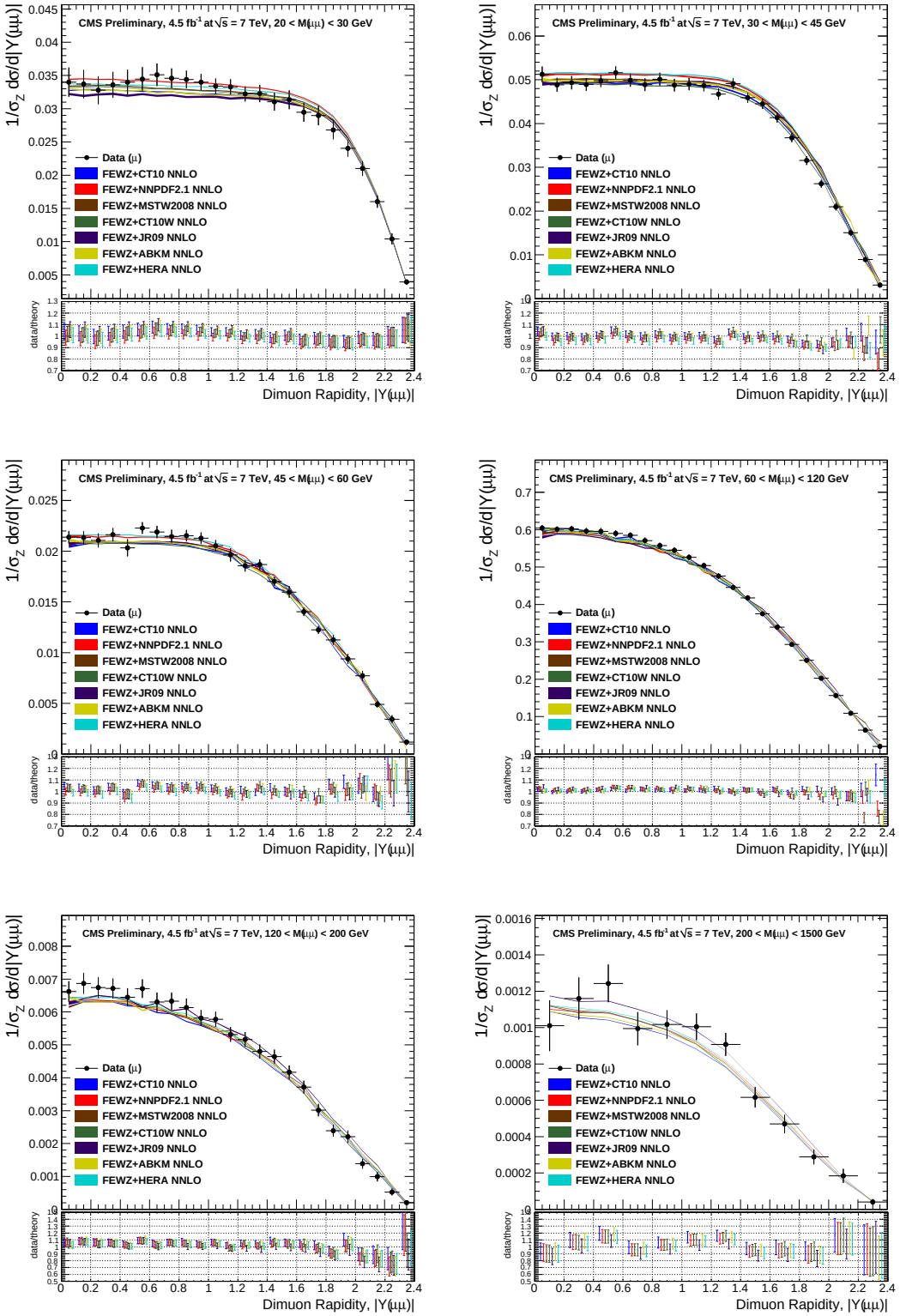

Figure 7: Comparison with theory expectations using various PDF sets. The error bands in the theory predictions indicate the statistical calculation error only. Bottom plot shows the ratio of data to theory expectation. The error bar is the quadrature sum of experimental uncertainty in the data and statistical calculation error on theory expectation.

These double-differential Drell-Yan measurements will impose constraints on the quark and anti-quark PDFs in a wide range of x, and in particular, will allow the replacement of old fixed target DY data with modern collider data in global PDF analysis.

6 Summary

This paper presents measurements of the Drell-Yan differential cross section $d\sigma/dM$ in the dimuon and dielectron channels for the mass range $15 < M < 1500$ GeV and the double-differential cross section $d^2\sigma/dMdY$ in the dimuon channel for the mass range $20 < M < 1500$ GeV.

The differential cross section measurements are normalized to the Z-peak region (60 – 120 GeV), which cancels out the uncertainty in the integrated luminosity and reduces the PDF uncertainty in acceptance, the pileup effect in the reconstruction efficiency and the uncertainty in the efficiency estimation. The measurements are corrected for the effects of resolution which cause event migration between bins in mass and rapidity. The observed dilepton mass is also corrected for FSR due to the leptons radiating photons and changing the dilepton invariant mass. This effect is most pronounced below the Z-peak. The $d\sigma/dM$ differential cross-section results are given separately for both lepton flavours in the fiducial region and are extrapolated to the full phase space. The consistency of the electron and muon results enables these to be combined for a precise comparison with the NNLO QCD predictions with FEWZ [6] using CT10 PDF. There is excellent agreement with the NNLO theoretical predictions.

The $d^2\sigma/dMdY$ measurement is compared to the NLO prediction calculated with FEWZ using CT10 PDF and the NNLO theoretical predictions as computed with FEWZ using the CT10, NNPDF2.1, MSTW2008, HERAPDF, JR09, ABKM and CT10W PDFs [13]. These precise results will provide valuable input to update the PDF sets and extend our knowledge of perturbative QCD and the partonic contents of the proton.

Acknowledgments

We would like to thank the authors of FEWZ and POWHEG for the fruitful discussions, cooperation, and cross-checks in performing the theoretical calculations for our analysis.

We wish to congratulate our colleagues in the CERN accelerator departments for the excellent performance of the LHC machine. We thank the technical and administrative staff at CERN and other CMS institutes. This work was supported by the Austrian Federal Ministry of Science and Research; the Belgium Fonds de la Recherche Scientifique, and Fonds voor Wetenschappelijk Onderzoek; the Brazilian Funding Agencies (CNPq, CAPES, FAPERJ, and FAPESP); the Bulgarian Ministry of Education and Science; CERN; the Chinese Academy of Sciences, Ministry of Science and Technology, and National Natural Science Foundation of China; the Colombian Funding Agency (COLCIENCIAS); the Croatian Ministry of Science, Education and Sport; the Research Promotion Foundation, Cyprus; the Estonian Academy of Sciences and NICPB; the Academy of Finland, Finnish Ministry of Education and Culture, and Helsinki Institute of Physics; the Institut National de Physique Nucléaire et de Physique des Particules / CNRS, and Commissariat à l'Énergie Atomique et aux Énergies Alternatives / CEA, France; the Bundesministerium für Bildung und Forschung, Deutsche Forschungsgemeinschaft, and Helmholtz-Gemeinschaft Deutscher Forschungszentren, Germany; the General Secretariat for Research and Technology, Greece; the National Scientific Research Foundation, and National Office for Research and Technology, Hungary; the Department of Atomic Energy and the Department

of Science and Technology, India; the Institute for Studies in Theoretical Physics and Mathematics, Iran; the Science Foundation, Ireland; the Istituto Nazionale di Fisica Nucleare, Italy; the Korean Ministry of Education, Science and Technology and the World Class University program of NRF, Korea; the Lithuanian Academy of Sciences; the Mexican Funding Agencies (CINVESTAV, CONACYT, SEP, and UASLP-FAI); the Ministry of Science and Innovation, New Zealand; the Pakistan Atomic Energy Commission; the State Commission for Scientific Research, Poland; the Fundação para a Ciência e a Tecnologia, Portugal; JINR (Armenia, Belarus, Georgia, Ukraine, Uzbekistan); the Ministry of Science and Technologies of the Russian Federation, the Russian Ministry of Atomic Energy and the Russian Foundation for Basic Research; the Ministry of Science and Technological Development of Serbia; the Ministerio de Ciencia e Innovación, and Programa Consolider-Ingenio 2010, Spain; the Swiss Funding Agencies (ETH Board, ETH Zurich, PSI, SNF, UniZH, Canton Zurich, and SER); the National Science Council, Taipei; the Scientific and Technical Research Council of Turkey, and Turkish Atomic Energy Authority; the Science and Technology Facilities Council, UK; the US Department of Energy, and the US National Science Foundation.

Individuals have received support from the Marie-Curie programme and the European Research Council (European Union); the Leventis Foundation; the A. P. Sloan Foundation; the Alexander von Humboldt Foundation; the Associazione per lo Sviluppo Scientifico e Tecnologico del Piemonte (Italy); the Belgian Federal Science Policy Office; the Fonds pour la Formation à la Recherche dans l'Industrie et dans l'Agriculture (FRIA-Belgium); the Agentschap voor Innovatie door Wetenschap en Technologie (IWT-Belgium); and the Council of Science and Industrial Research, India.

References

[1] S. Catani et al., "Vector boson production at hadron colliders: a fully exclusive QCD calculation at NNLO", *Phys. Rev. Lett.* **103** (2009) 082001, doi:10.1103/PhysRevLett.103.082001.

[2] S. Catani and M. Grazzini, "An NNLO subtraction formalism in hadron collisions and its application to Higgs boson production at the LHC", *Phys. Rev. Lett.* **98** (2007) 222002, doi:10.1103/PhysRevLett.98.222002.

[3] K. Melnikov and F. Petriello, "Electroweak gauge boson production at hadron colliders through $O(\alpha_s^2)$", *Phys. Rev. D* **74** (2006) 114017, doi:10.1103/PhysRevD.74.114017.

[4] R. D. Ball et al., "A first unbiased global NLO determination of parton distributions and their uncertainties", *Nucl.Phys.* **B838** (2010) 136–206, doi:10.1016/j.nuclphysb.2010.05.008, arXiv:1002.4407.

[5] S. Alioli et al., "NLO vector-boson production matched with shower in POWHEG", *JHEP* **0807** (2008) 060, doi:10.1088/1126-6708/2008/07/060, arXiv:0805.4802.

[6] R. Gavin et al., "FEWZ 2.0: A code for hadronic Z production at next-to-next-to-leading order", *Comput. Phys. Commun.* **182** (2011) 2388.

[7] H.-L. Lai et al., "New parton distributions for collider physics", *Phys. Rev.* **D82** (2010) 074024, doi:10.1103/PhysRevD.82.074024, arXiv:1007.2241.

[8] R. D. Ball et al., "Impact of Heavy Quark Masses on Parton Distributions and LHC Phenomenology", *Nucl. Phys.* **B849** (2011) 296, doi:10.1016/j.nuclphysb.2011.03.021, arXiv:1101.1300.

[9] A. Martin et al., "Parton distributions for the LHC", *Eur. Phys. J.* **C63** (2009) 189, doi:10.1140/epjc/s10052-009-1072-5, arXiv:0901.0002.

[10] H1 and ZEUS Collaboration, "Combined Measurement and QCD Analysis of the Inclusive $e^{\pm}p$ Scattering Cross Sections at HERA", *JHEP* **1001** (2010) 109, doi:10.1007/JHEP01(2010)109, arXiv:0911.0884.

[11] P. Jimenez-Delgado and E. Reya, "Dynamical NNLO parton distributions", *Phys. Rev.* **D79** (2009) 074023, doi:10.1103/PhysRevD.79.074023, arXiv:0810.4274.

[12] S. Alekhin et al., "The 3, 4, and 5-flavor NNLO Parton from Deep-Inelastic-Scattering Data and at Hadron Colliders", *Phys. Rev.* **D81** (2010) 014032, doi:10.1103/PhysRevD.81.014032, arXiv:0908.2766.

[13] S. Alekhin et al., "The PDF4LHC Working Group Interim Report", arXiv:1101.0536.

[14] CMS Collaboration, "The CMS experiment at the CERN LHC", *JINST* **3** (2008) S08004, doi:10.1088/1748-0221/3/08/S08004.

[15] CMS Collaboration, "The TriDAS Project Technical Design Report, volume I: The trigger systems", *CMS TDR CERN/LHCC 2000-038* (2000).

[16] CMS Collaboration, "The TriDAS Project Technical Design Report, volume II: Data acquisition and high-level trigger", *CMS TDR CERN/LHCC 2002-026* (2002).

[17] GEANT4 Collaboration, "GEANT4: A simulation toolkit", *Nucl. Instrum. Meth.* **A506** (2003) 250, doi:10.1016/S0168-9002(03)01368-8.

[18] T. Sjöstrand, S. Mrenna, and P. Z. Skands, "PYTHIA 6.4 Physics and Manual", *JHEP* **0605** (2006) 026, arXiv:hep-ph/0603175.

[19] J. Alwall et al., "MadGraph v5: going beyond", *JHEP* **1106** (2011) 128.

[20] Z. Was et al., "TAUOLA the library for tau lepton decay", *Nucl. Phys. Proc. Suppl.* **98** (2001) 96, doi:10.1016/S0920-5632(01)01200-2.

[21] R. Field, "Min-Bias and the Underlying Event at the LHC", *Acta Phys. Polon. B* **42** (2011) 2631.

[22] CMS Collaboration, "Performance of muon identification in pp collisions at $\sqrt{s} = 7$ TeV", *CMS Physics Analysis Summary CMS-PAS-MUO-10-002* (2010).

[23] CMS Collaboration, "Particle-flow commissioning with muons and electrons from J/ψ and W events at 7 TeV", *CMS Physics Analysis Summary CMS-PAS-PFT-10-003* (2010).

[24] S. Baffioni et al., "Electron reconstruction in CMS", *Eur. Phys. J.* **C49** (2007) 1099, doi:10.1140/epjc/s10052-006-0175-5.

[25] CMS Collaboration, "Measurement of the W and Z inclusive production cross sections at $\sqrt{s} = 7$ TeV with the CMS experiment at the LHC", *JHEP* **1101** (2011) 080, doi:10.1007/JHEP01(2011)080.

[26] A. Bodek, A. van Dyne, J.Y. Han, W. Sakumoto, and A. Strelnikov, "Extracting muon momentum scale corrections for hadron collider experiments", *Eur. Phys. J. C 72, 2194* (2012).

[27] V. Blobel, "An unfolding method for high-energy physics experiments", arXiv:hep-ex/0208022.

[28] CMS Collaboration, "Measurement of the Drell-Yan Cross Section in pp Collisions at $\sqrt{s} = 7$ TeV", *JHEP* **1110** (2011) 007, doi:10.1007/JHEP10(2011)007.

[29] CMS Collaboration, "Update of the measurement of Drell-Yan cross section in pp collisions at $\sqrt{s} = 7$ TeV with 1.1 fb^{-1} of 2011 data", *CMS Physics Analysis Summary CMS-PAS-EWK-11-020* (2011).

[30] H. Burkhardt and B. Pietrzyk, "Update of the hadronic contribution to the QED vacuum polarization", *Phys. Lett. B* **513** (2001) 46.

[31] D. Bourilkov, "Study of parton density function uncertainties with LHAPDF and PYTHIA at LHC", arXiv:hep-ph/0305126.

[32] M. Whalley, D. Bourilkov, and R. Group, "The Les Houches accord PDFs (LHAPDF) and LHAGLUE", arXiv:hep-ph/0508110.

[33] D. Bourilkov, R. C. Group, and M. R. Whalley, "LHAPDF: PDF use from the Tevatron to the LHC", arXiv:hep-ph/0605240.

[34] G. Lafferty and T. Wyatt, "Where to Stick Data Points: The Treatment of Measurements Within Wide Bins", *Nucl. Instr. Meth.* **A335** (1995) 541, doi:10.1016/0168-9002(94)01112-5.

[35] Y. Li and F. Petriello, "Combining QCD and electroweak corrections to dilepton production in FEWZ", *Phys.Rev.* **D86** (2012) 094034.

[36] A. Valassi, "Combining correlated measurements of several different physical quantities", *Nucl. Instrum. Meth. A* **500** (2003) 391, doi:10.1016/S0168-9002(03)00329-2.

[37] T. Aaltonen et al., "Direct Measurement of the W Production Charge Asymmetry in Collisions at $\sqrt{s} = 1.96$ TeV", *Phys. Rev. Lett.* **102** (2009) 181801.

[38] M. Klein and R. Yoshida, "Collider physics at HERA", *Progress in Particle and Nuclear Physics* **61** (2008) 343.

[39] L. Whitlow et al., "Precise measurements of the proton and deuteron structure functions from a global analysis of the SLAC deep inelastic electron scattering cross sections", *Phys. Lett. B* **282** (1992) 475.

[40] G. Moreno et al., "Dimuon production in proton-copper collisions at $\sqrt{s} = 38.8$ GeV", *Phys. Rev. D* **43** (1991) 2815.

[41] R. Towell et al., "Improved measurement of the $\bar{d}/\bar{u}$ asymmetry in the nucleon sea", *Phys. Rev. D* **64** (2001) 052002.